

# Multivariate Time-Series Anomaly Detection with Contaminated Data: Application to Physiological Signals

Thi Kieu Khanh Ho \*, Narges Armanfard

Department of Electrical and Computer Engineering, McGill University  
Mila - Quebec AI Institute, Montreal, QC, Canada

## Abstract

Mainstream unsupervised anomaly detection algorithms often excel in academic datasets, yet their real-world performance is restricted due to the controlled experimental conditions involving clean training data. Addressing the challenge of training with noise, a prevalent issue in practical anomaly detection, is frequently overlooked. In a pioneering endeavor, this study delves into the realm of label-level noise within sensory time-series anomaly detection (TSAD). This paper presents a novel and practical end-to-end unsupervised TSAD when the training data are contaminated with anomalies. The introduced approach, called TSAD-C, is devoid of access to abnormality labels during the training phase. TSAD-C encompasses three modules: a Decontaminator to rectify the abnormalities (aka noise) present in the training data, a Variable Dependency Modeling module to capture both long-term intra- and inter-variable dependencies within the decontaminated data that can be considered as a surrogate of the pure normal data, and an Anomaly Scoring module to detect anomalies. Our extensive experiments conducted on three widely used physiological datasets conclusively demonstrate that our approach surpasses existing methodologies, thus establishing a new state-of-the-art performance in the field.

## Introduction

Analyzing human disorders using multivariate physiological signals (MPS) is an important aspect of medical research and diagnostics. MPS are obtained from the human body recorded by sensory systems where a sensor is considered as a variable (James and Hesse 2004). MPS provide valuable information about the physiological states and the functions of the human body. For example, electrocardiogram (ECG) (Berkaya et al. 2018) involves placing sensors on the skin to measure the signals generated by the heart's contractions. ECG is an important modality to diagnose various cardiac disorders. Another example of MPS is electroencephalogram (EEG) (Tao et al. 2005), a neurophysiological test that measures the brain activity. EEG is obtained by placing sensors either on the scalp or within the brain and essential in epilepsy diagnosis, sleep monitoring and cognitive studies.

\*Corresponding Author (Email: thi.k.ho@mcgill.ca).

This paper has been submitted for possible publication. Copyright may be transferred without notice, after which this version may no longer be accessible.

Many machine learning methods have been proposed to automatically detect anomalies in MPS. For example, (Isin and Ozdalili 2017; Rath et al. 2021; Abubaker and Babayiğit 2022) aimed to detect abnormal rhythms and other irregular patterns in ECG. In EEG research, (Thodoroff, Pineau, and Lim 2016; Khalkhali et al. 2021; Rashed-Al-Mahfuz et al. 2021; Thuwajit et al. 2021; Tang et al. 2021, 2023; Ho and Armanfard 2023) aimed to detect abnormal epileptic activities, called seizures, while (Jia et al. 2020; Loh et al. 2022; Xu et al. 2022; Ettahiri, Ferrández Vicente, and Fectali 2022) proposed to detect sleep-related disorders. However, several major concerns still remain unsolved.

First, the majority of these MPS studies trained their models in a supervised way, i.e., both labeled normal and abnormal samples are available in the training phase; or in a semi-supervised way, when a few labeled abnormal samples are available. This does not address the challenge from a clinical point of view as abnormal activities are very difficult to obtain due to the time-consuming, costly and labor-intensive process for accurately labelling anomalous patterns. Several recent MPS studies have successfully tackled this issue by proposing an unsupervised approach, i.e., only normal data is available in the training phase. However, in many real-world applications, anomalies often sneak into normal data, which comes from the data shift or human misjudgment (Jiang et al. 2022). Existing unsupervised methods are sensitive to the seen anomalies due to their exhaustive strategy to model the normal training data, hence, they would misdetect similar anomaly samples in the test phase. Therefore, developing a method that can detect anomalies while being trained on contaminated data is necessary, yet there is no method that has aimed to tackle this challenge in MPS.

Second, it is important to capture both intra-variable (aka temporal) and inter-variable (aka spatial) dependencies in the time series (Ho, Karami, and Armanfard 2023). However, existing unsupervised studies are unable to effectively capture both dependencies in MPS. Regarding the intra-variable dependencies, they often preprocessed data by segmenting the signals into short time intervals (Strodthoff et al. 2020; Pradhan, He, and Jiang 2022), or applied traditional temporal networks such as recurrent neural networks or transformers (Lim et al. 2021; Katharopoulos et al. 2020). Such learned dependencies imply that observations close to each other are expected to be similar. However, trends, sea-

sonality and unpredictability are always present in the time series, hence, learning the short-term dependencies is problematic. Thus, developing a method that can handle the long-range intra-variable dependencies in MPS is crucial.

Regarding the inter-variable dependencies, very recently, graphs have brought a potential to model the relationships between variables (sensors) in time-series data. By representing variables as nodes and their connections as edges, graphs provide an intuitive way to understand the underlying relationships between variables. However, modeling graphs to effectively capture this type of dependencies in MPS is challenging. Existing MPS studies proposed to pre-define graphs based on prior knowledge, e.g., the known locations of sensors (Tang et al. 2021). However, it is not feasible in many MPS applications, where the exact locations of sensors may vary among patients due to the variability of the chest/head size, the suspicious abnormal regions and the clinical need. Therefore, instead of pre-defining graphs, dynamically learning the graph structure and features over-time, is highly desirable.

Lastly, while long-range intra- and inter-variable dependencies are both important for MPS, designing an effective joint learning framework to capture both dependencies is yet challenging. Recent studies have shown that there are two groups of a combined model: time-and-graph and time-then-graph (Gao and Ribeiro 2022). A time-and-graph approach first constructs graphs and then embeds a temporal network. On the other hand, a time-then-graph framework first projects time-series data to a temporal network, the extracted temporal features are then used to model graphs. It is shown that compared to a time-and-graph framework, a time-then-graph approach achieves a significant improvement in classification and regression tasks (Gao and Ribeiro 2022; Tang et al. 2023). However, till now, there is no study that has explored the time-then-graph framework for unsupervised anomaly detection tasks in MPS.

Based on the above observations, we propose a novel approach for anomaly detection, called TSAD-C. The main contributions of this paper are described as follows:

- We propose a novel approach, namely TSAD-C, trained on contaminated data in an end-to-end manner to detect anomalies in MPS. To the best of our knowledge, this is the first study that uses contaminated data in the training phase for TSAD, addressing a much more challenging problem than the existing studies.
- TSAD-C is comprised of three primary modules: the Decontaminator, the Variable Dependency Modeling, and the Anomaly Scoring module. The initial module aims to identify and eliminate abnormal patterns that are likely to be anomalies. The second module is to model the long-term intra- and inter-variable dependencies. The last module computes anomaly scores to detect anomalies.
- The Decontaminator leverages masking strategies and an S4-based conditional diffusion model, while the Variable Dependency Modeling module integrates structured state spaces (S4) layers, a graph learning strategy and graph isomorphism network (GIN) layers. The Anomaly Scoring module is defined by leveraging the insights of the

first two modules.

- We perform extensive experiments on three widely used MPS datasets and demonstrate that our method outperforms existing studies and thus establishes a new state-of-the-art in the field.

## Proposed Method

A dataset is defined as  $X = (\mathbf{x}_{(1)}, \mathbf{x}_{(2)}, \dots, \mathbf{x}_{(N)})$ , where  $\mathbf{x}_{(i)} = (x_{(i)}^1, x_{(i)}^2, \dots, x_{(i)}^K)$  is the  $i$ th observation in the time series of  $N$  observations,  $\mathbf{x}_{(i)} \in \mathbb{R}^{K \times L}$ ,  $K$  and  $L$  denote the number of variables (sensors) and the length of the  $i$ th observation, respectively. An observation can be conceptualized as  $L$  samples collected from  $K$  sensors over the  $i$ th time interval. Our task is to detect anomalous observations in the test data (i.e.,  $X_{\text{test}}$ ) by training the model with contaminated normal data (i.e.,  $X_{\text{train}}$ ). Note that, during the training phase, no information about the outlier data that contaminates the normal data is provided, such as their labels or their positions within the time series. We use a validation set (i.e.,  $X_{\text{valid}}$ ) for early stopping and finding the decision threshold. The block diagram of the proposed TSAD-C method, depicting the three modules, namely Decontaminator, Variable Dependency Modeling, and Anomaly Scoring, is shown in Figure 1. Details of each module are presented below.

### Decontaminator

**Masking Strategies.** Following the practical scenarios when collecting normal data, in this paper, we assume that the number of normal samples significantly outweighs the number of abnormal events. Considering this assumption, when we mask a portion of  $X_{\text{train}}$ , there is a likelihood of removing both abnormal and normal patterns. Nonetheless, due to the predominant presence of normal data in  $X_{\text{train}}$ , the omission of certain normal patterns is not likely to yield detrimental consequences as the substantial amount of remaining normal data can adequately compensate for the masked portions. Conversely, the act of masking has the advantageous outcome of diminishing the proportion of anomalies. This effect is beneficial for the downstream module as it facilitates the learning process of variable dependencies that characterize the underlying behavior of normality.

We define a binary mask as  $\mathbf{v} \in \{0, 1\}$ ,  $\mathbf{v} \in \mathbb{R}^{K \times L}$ , where zeros denote the values to be masked and the values to be kept are marked by ones. Hence, the  $i$ th masked observation is  $\mathbf{x}_{(i)}^u = \mathbf{x}_{(i)} \odot \mathbf{v}$ , where  $\mathbf{x}_{(i)}^u \in \mathbb{R}^{K \times L}$  and  $\odot$  denotes point-wise multiplication. Following the current literature of masking techniques in the time-series domain (Khayati et al. 2020; Alcaraz and Strodthoff 2022), we perform three popular masking scenarios, namely random masking (RandM), random block masking (RandBM) and blackout masking (BoM). A hyper-parameter, called the number of time stamps  $r$ , is assigned for three masking methods. RandM randomly samples  $r$  to be masked across variables (sensors). For RandBM and BoM, we partition  $\mathbf{x}_{(i)}$  into non-overlapping segments, and each segment has the size of  $r$ . While RandBM randomly samples a segment in the pool of segments to be masked across variables, BoM samples the same segment to be masked across all variables.

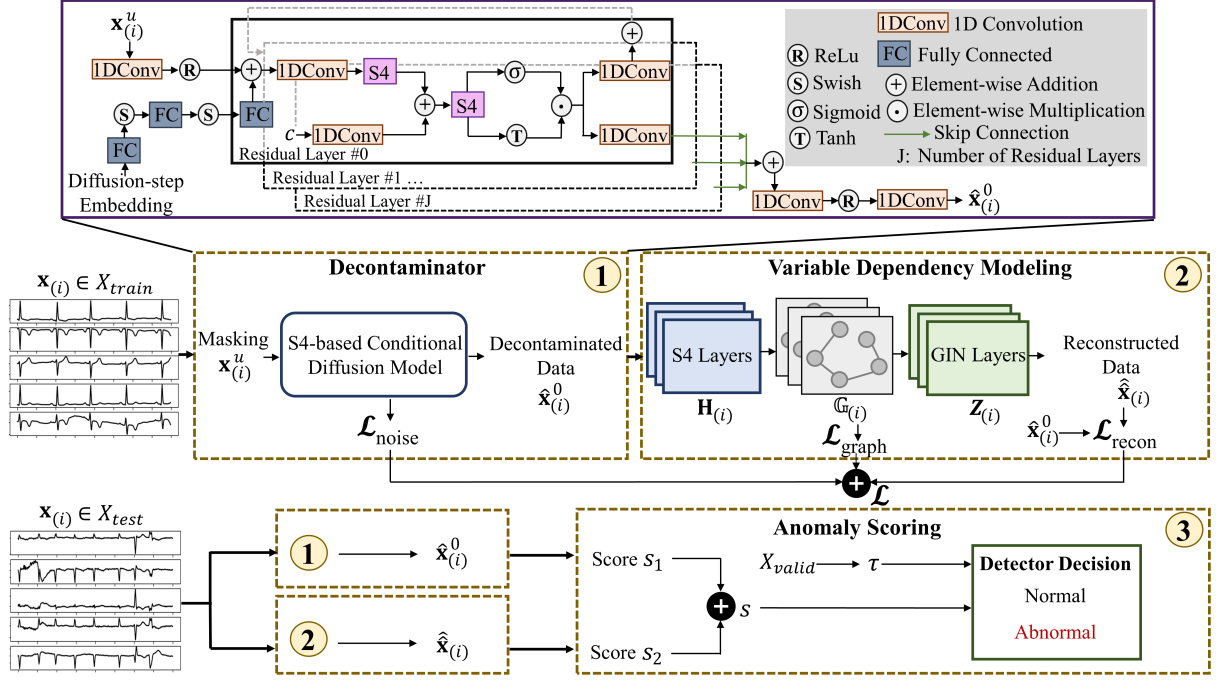


Figure 1: The overall framework of TSAD-C.

**S4-based Conditional Diffusion Model.** This module is developed based on a diffusion model, a class of generative models inspired by non-equilibrium thermodynamics (Sohl-Dickstein et al. 2015). It defines a two-process paradigm, including the diffusion and reserve processes. In this paper, the diffusion process, defined by a Markov chain, incrementally adds Gaussian noise to the initial stage of  $\mathbf{x}_{(i)}^u$ , called  $\mathbf{x}_{(i)}^0$ , over  $T$  diffusion steps and can be represented as:

$$p(\mathbf{x}_{(i)}^1, \dots, \mathbf{x}_{(i)}^T | \mathbf{x}_{(i)}^0) = \prod_{t=1}^T p(\mathbf{x}_{(i)}^t | \mathbf{x}_{(i)}^{t-1}), \quad (1)$$

where  $p(\mathbf{x}_{(i)}^t | \mathbf{x}_{(i)}^{t-1}) := \mathcal{N}(\mathbf{x}_{(i)}^t; \mu_{(i)}^t, \sigma_{(i)}^t)$ . This indicates  $\mathbf{x}_{(i)}^t$  is sampled from a normal distribution with mean  $\mu_{(i)}^t = \sqrt{1 - \beta_t} \mathbf{x}_{(i)}^{t-1}$  and variance  $\sigma_{(i)}^t = \beta_t \mathbf{I}$ .  $\mathbf{I}$  is the identity matrix,  $\beta_t \in (0, 1)$  is a variance schedule that controls the quantity of noise added at the  $t$ th diffusion step. In our implementation, we increase  $\beta_t$  linearly from  $10^{-4}$  to 0.02. By setting  $\alpha_t = 1 - \beta_t$ ,  $\bar{\alpha}_t = \prod_{j=1}^t \alpha_j$ , the diffusion process allows to immediately transform  $\mathbf{x}_{(i)}^0$  to a noisy  $\mathbf{x}_{(i)}^t$  according to  $\beta_t$  in a closed form as  $\mathbf{x}_{(i)}^t = \sqrt{\bar{\alpha}_t} \mathbf{x}_{(i)}^0 + \sqrt{1 - \bar{\alpha}_t} \epsilon_t$  where the noise  $\epsilon_t \sim \mathcal{N}(0, \mathbf{I})$ ,  $\epsilon_t \in \mathbb{R}^{K \times L}$ . We add noise to both masked and non-masked portions of  $\mathbf{x}_{(i)}^0$ . As the diffusion step increases,  $\mathbf{x}_{(i)}^t$  gradually loses its distinguishable features and approaches a Gaussian distribution; hence, both anomalous and normal patterns appear indistinguishable.

The reverse process defined by a Markov chain is param-

eterized by  $\theta$  and can be represented as:

$$q_{\theta}(\mathbf{x}_{(i)}^0, \dots, \mathbf{x}_{(i)}^{T-1} | \mathbf{x}_{(i)}^T) = \prod_{t=1}^T q_{\theta}(\mathbf{x}_{(i)}^{t-1} | \mathbf{x}_{(i)}^t), \quad (2)$$

where each  $q_{\theta}(\mathbf{x}_{(i)}^{t-1} | \mathbf{x}_{(i)}^t) := \mathcal{N}(\mathbf{x}_{(i)}^{t-1}; \mu_{\theta}(\mathbf{x}_{(i)}^t, t, c), \sigma_{\theta}(\mathbf{x}_{(i)}^t, t, c)^2 \mathbf{I})$ .  $\mu_{\theta}$  and  $\sigma_{\theta}$  are parameterized as:

$$\begin{aligned} \mu_{\theta}(\mathbf{x}_{(i)}^t, t, c) &= \frac{1}{\sqrt{\alpha_t}} \left( \mathbf{x}_{(i)}^t - \frac{\beta_t}{\sqrt{1 - \bar{\alpha}_t}} \epsilon_{\theta}(\mathbf{x}_{(i)}^t, t, c) \right), \\ \sigma_{\theta}(\mathbf{x}_{(i)}^t, t, c) &= \sqrt{\bar{\beta}_t}, \end{aligned} \quad (3)$$

where  $\bar{\beta}_t = \frac{1 - \bar{\alpha}_{t-1}}{1 - \bar{\alpha}_t} \beta_t$  and  $\bar{\beta}_1 = \beta_1$ .  $\epsilon_{\theta}$  is a network approximator, which takes  $\mathbf{x}_{(i)}^t$ , the diffusion step  $t$  and a conditional factor  $c$  as the inputs and aims to predict the noise from  $\mathbf{x}_{(i)}^t$ . Note that compared to the unconditional diffusion models, conditional cases typically achieve a better performance as the reverse process is conditioned on additional information (Alcaraz and Strothoff 2022). In our scenario,  $c$  is a concatenation of the non-masked segments in  $\mathbf{x}_{(i)}^u$  and the positional information of the masked parts provided by  $\mathbf{v}$ . With this extra information, it facilitates the reverse process to distinguish the zero portions of non-masked and masked parts. It is worth mentioning that  $\epsilon_{\theta}$  has an important role in the reverse process. U-Net-like architectures, based on PixelCNN and ResNet, are typically utilized to build  $\epsilon_{\theta}$  for anomaly detection in the image domain (Zhang et al. 2023). However, in the time-series domain, capturing long-range intra-variable dependencies is crucial. Hence, we propose to build  $\epsilon_{\theta}$  based on a recently proposed deep sequence model, called S4 (Gu, Goel, and Ré 2022). S4 is basically based on the concept of

a state space model (SSM). A continuous-time SSM maps  $\mathbf{x}_{(i)}^t$  to a high dimensional state  $h_{(i)}^t$  before projecting it to the output  $\mathbf{y}_{(i)}^t$ . This transition can be defined as:

$$\tilde{h}_{(i)}^t = Ah_{(i)}^t + B\mathbf{x}_{(i)}^t \text{ and } \mathbf{y}_{(i)}^t = Ch_{(i)}^t + D\mathbf{x}_{(i)}^t, \quad (4)$$

where  $A, B, C, D$  are transition matrices learned by gradient descent. S4 shows that a discrete-time SSM can be represented as a convolution operation by:

$$\bar{O} := (\overline{CB}, \overline{CAB}, \dots, \overline{CA}^{L-1}\overline{B}), \mathbf{y}_{(i)} = \bar{O} * \mathbf{x}_{(i)}, \quad (5)$$

where  $\bar{A}, \bar{B}, \bar{C}$  are the discretized matrices,  $\overline{CA}^{L-1}$  denotes the multiplication of discretized matrices at  $L-1$ , and  $\bar{O}$  is a SSM convolution kernel. Note that  $D$  is omitted in Equation (5) as  $D\mathbf{x}_{(i)}^t$  can be viewed as a skip connection. Essentially, S4 parameterizes  $A$  as a diagonal plus low rank matrix and this parameterization enables fast computation of  $\bar{O}$ . Moreover, it includes the HiPPO matrices (Gu et al. 2020), which are a series of matrices that is capable of capturing long-term intra-variable dependencies. Our Decontaminator module employs two S4 layers, one after the addition of the embeddings related to  $\mathbf{x}_{(i)}^u$  and another layer after including  $c$  in the residual blocks (see Figure 1).

For a simpler and more streamlined reverse process during the training of  $\epsilon_\theta$  for noise estimation, we suggest minimizing the noise error specifically on the masked segments, as illustrated in Equation (6). It is important to highlight that the masked parts solely consist of noise without any underlying data pattern, unlike the non-masked parts which contain both noise and the actual data pattern. Consequently, deriving noise estimates from the masked data is a more straightforward task and can be accomplished using less intricate networks. This approach is advantageous as it facilitates swift data preparation for the subsequent module.

$$\mathcal{L}_{\text{noise}} = \|\epsilon_t \odot (1 - M) - \hat{\epsilon}_t \odot (1 - M)\|^2, \quad (6)$$

where  $\hat{\epsilon}_t$  is the predicted noise obtained from  $\epsilon_\theta(\mathbf{x}_{(i)}^t, t, c)$ .

We obtain decontaminated data in the training phase as:

$$\hat{\mathbf{x}}_{(i)}^0 = \frac{1}{\sqrt{\bar{\alpha}_T}} \left( \mathbf{x}_{(i)}^T - \sqrt{1 - \bar{\alpha}_T} \hat{\epsilon}_T \right). \quad (7)$$

Note that approximating  $\hat{\mathbf{x}}_{(i)}^0$  immediately at the  $T$ th step allows us to have a faster reverse speed in the training phase as  $\hat{\mathbf{x}}_{(i)}^0$  will be used as the input for the second module in the training framework. On the other hand, in the test phase, we perform a complete sampling step from  $T$  to 1 in the reverse process according to Equations (2) and (3) to obtain  $\hat{\mathbf{x}}_{(i)}^0$ .

## Variable Dependency Modeling

In this module, we aim to build a time-then-graph framework, as is motivated in the Introduction, by including multiple back-to-back S4 layers to capture intra-variable dependencies, a graph learning strategy to dynamically learn the graph structure and features, and GIN layers (Xu et al. 2019) to capture inter-variable dependencies.

Regarding the S4 layers, we use  $\hat{\mathbf{x}}_{(i)}^0 \in \mathbb{R}^{K \times L}$  as the input and project it onto an embedding space, called  $\mathbf{H}_{(i)}$   $\in$

$\mathbb{R}^{K \times \Gamma \times U}$ , where  $\Gamma$  and  $U$  are hyper-parameters defining the S4 embedding dimension. In our experiments, to maintain a sense of the number of time stamps present in  $\mathbf{x}_{(i)}$ , we set  $\Gamma$  to  $L$ , corresponding to the length of the input time series. This allows us to model the long-term intra-variable dependencies within each variable.  $\mathbf{H}_{(i)}$  is used as the input to the graph learning phase, which models the underlying inter-variable dependencies. Prior studies have shown the superior performance of graph learning when using the temporal embedding rather than the original data (Tang et al. 2023).

Regarding the graph learning phase, we represent  $\mathbf{H}_{(i)}$  as a set of graphs  $\mathbb{G}_{(i)} = \{\mathcal{G}_{(i)}^m\}_{m=1}^d$ , where  $d = \frac{\Gamma}{g}$  and  $g$  is the pre-defined length of the short and non-overlapping time intervals within the  $i$ th observation. As each observation within a dataset can encompass thousands of time stamps, constructing a graph for every individual time step becomes inefficient and computationally demanding. A more effective approach involves creating a graph over a defined time interval, which aids in information aggregation. This strategy not only leads to a graph with reduced noise but also facilitates faster computations (Gao and Ribeiro 2022).

We define  $\mathcal{G}_{(i)}^m = \{\mathbf{E}_{(i)}^m, \mathcal{A}_{(i)}^m\}$ . Here,  $\mathbf{E}_{(i)}^m \in \mathbb{R}^{K \times U}$  represents the embedding derived by averaging the elements of  $\mathbf{H}_{(i)}$  along its second dimension, and  $\mathcal{A}_{(i)}^m \in \mathbb{R}^{K \times K}$  is the adjacency matrix. Each row and column in  $\mathcal{A}_{(i)}^m$  corresponds to a node (i.e., variable). The non-zero value in the entry of  $\mathcal{A}_{(i)}^m$  indicates that there exists an edge connecting the two corresponding nodes. To determine the edge weights, we employ a self-attention paradigm (Vaswani et al. 2017; Tang et al. 2023) in which attention weights are assigned to the edges' magnitudes. This process can be formulated as:

$$\begin{aligned} \mathbf{Q} &= \mathbf{E}_{(i)}^m \mathbf{W}^{\mathbf{Q}}, \mathbf{R} = \mathbf{E}_{(i)}^m \mathbf{W}^{\mathbf{R}}, \\ \mathcal{A}_{(i)}^m &= \text{softmax}\left(\frac{\mathbf{Q}\mathbf{R}^\top}{\sqrt{D}}\right), \end{aligned} \quad (8)$$

where  $\mathbf{W}^{\mathbf{Q}}, \mathbf{W}^{\mathbf{R}} \in \mathbb{R}^{U \times U}$  are the learnable weights that project  $\mathbf{E}_{(i)}^m$  to the query  $\mathbf{Q}$  and the key  $\mathbf{R}$ , respectively.

In addition to the learnable parameters for creating the adjacency matrix  $\mathcal{A}_{(i)}^m$ , we include another pre-defined adjacency matrix, called  $\mathcal{A}'_{(i)}^m$  based  $\delta$ -nearest neighbors to help guiding the graph learning process. Its edge magnitudes are computed by measuring the cosine similarity between the nodes' embeddings in  $\mathbf{E}_{(i)}^m$ . We only keep the top  $\delta$  edges that have the highest values for each node to avoid overly connected graphs. In all our experiments,  $\delta = 3$ . The final  $\mathcal{A}_{(i)}^m$  employed in the loss function is obtained as:

$$\mathcal{A}_{(i)}^m = \zeta \mathcal{A}'_{(i)}^m + (1 - \zeta) \mathcal{A}_{(i)}^m, \quad (9)$$

where  $\zeta \in [0, 1]$  is a hyper-parameter to balance the two contributing components.

Following the graph literature (Zhu et al. 2021), it is important to have a graph regularized, i.e., to encourage properties such as smoothness (i.e., the features should change smoothly between neighboring nodes), sparsity (i.e., avoiding to have an overly connected graph) and connectivity (i.e., avoiding to have a disconnected graph). Hence, we include

three constraints in the regularization loss as below:

$$\begin{aligned} \mathcal{L}_{\text{graph}} = & \frac{1}{d} \sum_{m=1}^d \xi_1 \mathcal{L}_{\text{smooth}}(\mathbf{E}_{(i)}^m, \mathcal{A}_{(i)}^m) + \\ & \xi_2 \mathcal{L}_{\text{sparse}}(\mathcal{A}_{(i)}^m) + \xi_3 \mathcal{L}_{\text{connect}}(\mathcal{A}_{(i)}^m), \end{aligned} \quad (10)$$

where  $\mathcal{L}_{\text{smooth}} = \frac{1}{K^2} \text{tr}(\mathbf{E}_{(i)}^{m\top} M_{\text{Lap}} \mathbf{E}_{(i)}^m)$ ,  $M_{\text{Lap}} = M_{\text{degree}} - \mathcal{A}_{(i)}^m$  is the Laplacian matrix,  $M_{\text{degree}}$  is the degree matrix of  $\mathcal{A}_{(i)}^m$ , and  $\text{tr}(\cdot)$  denotes the trace of the matrix.  $\mathcal{L}_{\text{sparse}} = \frac{1}{K^2} \|\mathcal{A}_{(i)}^m\|_F^2$  and  $\|\cdot\|_F$  is the Frobenius norm of the matrix.  $\mathcal{L}_{\text{connect}} = -\frac{1}{K} \mathbf{1}^\top \log(\mathcal{A}_{(i)}^m \cdot \mathbf{1})$ , and  $\mathbf{1} \in \mathbb{R}^{K \times 1}$  is a matrix of ones.  $\xi_1, \xi_2$  and  $\xi_3$  are hyper-parameters to balance the regularization terms in  $\mathcal{L}_{\text{graph}}$ .

Finally, we add GIN layers to capture inter-variable dependencies between nodes in  $\mathcal{G}_{(i)}^m$ . Note that GIN, a variant of graph neural networks (GNN), shows a strong representational power compared to other types of GNN. The embedding of nodes in  $\mathcal{G}_{(i)}^m$  is represented as  $\mathbf{z}_{(i)}^m := \text{GIN}(\mathbf{E}_{(i)}^m, \mathcal{A}_{(i)}^m)$ ,  $\mathbf{z}_{(i)}^m \in \mathbb{R}^{K \times g \times U}$ . We concatenate the node embeddings of all graphs within  $\mathbb{G}_{(i)}$  as  $\mathbf{Z}_{(i)} = \text{concat}(\mathbf{z}_{(i)}^1, \dots, \mathbf{z}_{(i)}^d)$ . A linear layer is then added to obtain reconstructed data  $\hat{\mathbf{x}}_{(i)}$ , i.e.,  $\hat{\mathbf{x}}_{(i)} := \text{Linear}(\mathbf{Z}_{(i)})$ ,  $\hat{\mathbf{x}}_{(i)} \in \mathbb{R}^{K \times L}$ . Thus, the reconstruction loss is denoted as:

$$\mathcal{L}_{\text{recon}} = \|\hat{\mathbf{x}}_{(i)}^0 - \hat{\mathbf{x}}_{(i)}\|^2. \quad (11)$$

The final loss in the training phase is defined as the total loss of all three losses from Equations (6), (10) and (11):

$$\mathcal{L} = \mathcal{L}_{\text{noise}} + \mathcal{L}_{\text{graph}} + \mathcal{L}_{\text{recon}}. \quad (12)$$

## Anomaly Scoring

In the test phase, we compute an anomaly score based root mean square error (RMSE) for each observation  $\mathbf{x}_{(i)}$ . More specifically, we project  $\mathbf{x}_{(i)}$  to the Decontaminator where masking strategies and the complete sampling step from  $T$  to 1 are applied to obtain  $\hat{\mathbf{x}}_{(i)}^0$ . If  $\mathbf{x}_{(i)}$  is an abnormal observation, the masked portions are expected to be inaccurately sampled. At the same time, instead of using  $\hat{\mathbf{x}}_{(i)}^0$  as the input for the second module as is done in the training phase,  $\mathbf{x}_{(i)}$  is directly used to obtain  $\hat{\mathbf{x}}_{(i)}$  in the test phase. The underlying assumption is that if  $\mathbf{x}_{(i)}$  is an anomaly, the second component with the goal of achieving the flawless reconstruction of normal patterns would be unable to reconstruct it. The final score  $s$  for each  $\mathbf{x}_{(i)}$  is computed as:

$$\begin{aligned} s_1 &= \left( \frac{1}{L} \sum_{l=1}^L \sum_{k=1}^K \left( (\hat{\mathbf{x}}_{(i)}^0 - \mathbf{x}_{(i)}) \odot (1 - M) \right)^2 \right)^{0.5}, \\ s_2 &= \left( \frac{1}{L} \sum_{l=1}^L \sum_{k=1}^K \left( \hat{\mathbf{x}}_{(i)} - \mathbf{x}_{(i)} \right)^2 \right)^{0.5}, \\ s &= \lambda_1 s_1 + \lambda_2 s_2, \end{aligned} \quad (13)$$

where  $s_1$  and  $s_2$  are, respectively, the RMSE scores obtained from the first and second modules.  $\lambda_1$  and  $\lambda_2$  are hyper-parameters to balance the scores of the two modules. In all our experiments,  $\lambda_1$  and  $\lambda_2$  are fixed for all datasets.

Dataset	$X_{\text{train}}$ (% Abn)	$X_{\text{valid}}$ (% Abn)	$X_{\text{test}}$ (% Abn)	$K$	$L$
ICBEB	910 (20.0%)	82 (20.7%)	222 (59.9%)	12	6,000
DODH	2515 (19.8%)	320 (21.8%)	310 (51.6%)	16	7,500
TUSZ	5275 (17.0%)	1055 (20.0%)	1581 (40.0%)	19	12,000

Table 1: The numbers of observations are shown in  $X_{\text{train}}$ ,  $X_{\text{valid}}$ ,  $X_{\text{test}}$  of each dataset. The percentages of abnormal data (Abn) is noted in parenthesis.  $K$  and  $L$  are, respectively, the number of variables and the length of an observation.

We perform a decision threshold search on  $X_{\text{valid}}$ , i.e, we select a decision threshold  $\tau$  that results in the highest F1-score while maintaining the reasonable scores of other evaluation metrics on  $X_{\text{valid}}$ . In the test phase, observations with  $s$  above  $\tau$  are detected as anomalies. Note that there is no overlap between  $X_{\text{train}}$ ,  $X_{\text{valid}}$ , and  $X_{\text{test}}$ .

## Experiments

### Experimental Settings

In this section, we introduce the datasets and the experimental setup in our study.

**Datasets.** We use three challenging MPS public datasets, namely ICBEB (Liu et al. 2018), DODH (Guillot et al. 2020) and TUSZ v1.5.2 (Shah et al. 2018). ICBEB is an ECG database including the normal heart rhythm and different types of abnormalities. We select five anomaly types, namely atrial fibrillation (AF), first-degree atrioventricular block (I-AVB), right bundle branch block (RBBB), premature ventricular contraction (PVC) and ST-segment elevation (STE). DODH is a sleep staging database recorded from healthy volunteers. We select N3, which is the deepest sleeping stage, as normal data since the brain activity during this stage has an identifiable pattern of delta waves; and body activities such as breathing and muscle tone rate decrease. Meanwhile, rapid eye movement (REM) and Awake stages are considered as abnormal since the brain activity during these periods rises up; and the body activities such as the eyes and the muscles increase. In TUSZ, resting-state brain activities are considered as normal while abnormal brain activities are two types of seizures (focal and generalized seizures). Details of each dataset are shown in Table 1.

**Baselines.** We compare the performance of TSAD-C against two streams of deep learning based methods in the MPS literature: (1) supervised methods that use labeled data in the training phase; and (2) unsupervised methods that are trained without using any labels. Both supervised and unsupervised categories include the methods applicable to capture either intra-, inter-, or both-variable dependencies.

Specifically, we select four supervised methods, namely long short-term memory (LSTM) (Wang et al. 2018), S4 (Gu, Goel, and Ré 2022), temporal GNN (TGNN) and GraphS4mer (GSmer<sub>(1)</sub>) (Tang et al. 2023). While LSTM and S4 can capture the intra-variable dependencies, TGNN and GSmer<sub>(1)</sub> can capture both-variable dependencies. Plus, we select four unsupervised methods, including LSTM-Autoencoder (LAE) (Wei et al. 2023), S4AE (which shares

the same framework as LAE, with the distinction that in S4AE, LSTM is replaced with S4), Graph Autoencoder (GAE) (Du et al. 2022), and GraphS4mer (GSmer<sub>(2)</sub>) (which maintains the same framework as GSmer<sub>(1)</sub>, except that the cross-entropy loss used in GSmer<sub>(1)</sub> is substituted with a reconstruction loss). LAE and S4AE capture intra-variable dependencies, while GAE and GSmer<sub>(2)</sub> capture inter-variable and both-variable dependencies, respectively.

To facilitate our ablation analysis, we introduce three variations of TSAD-C based on the computed anomaly score. TSAD-C<sub>(1)</sub>, TSAD-C<sub>(2)</sub> and TSAD-C<sub>(1,2)</sub>, respectively, denote the performances based on the anomaly score obtained from the decontaminator (i.e.,  $s_1$ ), the variable dependency modeling module (i.e.,  $s_2$ ) and both components (i.e.,  $s$ ).

**Performance Evaluation Metrics.** Given the utilization of the imbalanced datasets detailed in Table 1 across all methods, we employ three evaluation metrics, namely F1-score (F1), Recall (Rec), and Area Under the Precision-Recall curve (APR) (Davis and Goadrich 2006), to comprehensively assess the performance of each method.

## Experimental Results

The performances of TSAD-C and existing methods are shown in Table 2. We first compare the performances of TSAD-C’s three variations. TSAD-C<sub>(2)</sub>, which computes anomaly scores for entire observations, consistently outperforms TSAD-C<sub>(1)</sub>, which scores only masked parts. Note that in the Tables, all anomaly types are included in all subsets and BoM is used. TSAD-C<sub>(1)</sub> is attributed to the test phase, where the reverse process of the Decontaminator incorporates the full sampling step to generate masked portions based on neighboring values. Due to a high amount of abnormal time stamps in  $X_{\text{test}}$ , the sampling stage can provide reasonable estimates for masked parts aligning with anomalous time stamps in the observations. Consequently, achieving distinct anomaly scores for normal and abnormal samples is challenging. Conversely, the second module excels in capturing inherent patterns within normal data, leading to strong reconstruction of normal observations while leaving abnormal ones unreconstructed, yielding high reconstruction errors. Hence, distinguishing between normal and abnormal samples becomes easier. Importantly, we observe that integrating anomaly scores of the two modules (i.e., TSAD-C<sub>(1,2)</sub>) yields the highest F1 for all datasets. This shows that both components can complement each other to improve the model’s ability in detecting anomalies.

Table 2 shows that TSAD-C outperforms all existing MPS studies in F1 and establishes a new SOTA in the field. Note that F1 shows the harmonic mean of precision and recall that considers both false positives and false negatives. A higher F1 score indicates that the model has a better balance between correctly identifying positive samples (i.e., anomalies), while effectively avoiding false positives. It also confirms that we obtain a significant improvement in Rec (i.e., the ability to correctly identifies most of the abnormal instances) compared to the existing methods. This is an ideal scenario in medical diagnosis and clinical applications, where high F1 and Rec are often prioritized. The reason behind this preference is that the model can flag po-

	Method	Metric	ICBEB	DODH	TUSZ
Supervised	LSTM	F1	0.565	0.442	0
		{Rec; APR}	{0.424; 0.807}	{0.284; 0.896}	{0; 0.687}
	S4	F1	0.707	0.597	0.423
		{Rec; APR}	{0.575; 0.871}	{0.426; 0.912}	{0.305; 0.637}
TGNN	F1	0.165	0.652	0.559	
	{Rec; APR}	{0.090; 0.893}	{0.484; 0.899}	{0.517; 0.658}	
GSmer <sub>(1)</sub>	F1	0.510	0.655	0.567*	
	{Rec; APR}	{0.342; 0.879}	{0.487; 0.924}	{0.459; 0.672}	
Unsupervised	LAE	F1	0.668	0.603	0.546
		{Rec; APR}	{0.772; 0.749}	{0.834; 0.697}	{0.542; 0.637}
	S4AE	F1	0.694	0.613	0.552
		{Rec; APR}	{0.826; 0.764}	{0.856; 0.704}	{0.554; 0.641}
GAE	F1	0.673	0.385	0.482	
	{Rec; APR}	{0.780; 0.751}	{0.463; 0.535}	{0.437; 0.600}	
GSmer <sub>(2)</sub>	F1	0.659	0.571	0.550	
	{Rec; APR}	{0.727; 0.747}	{0.775; 0.672}	{0.767; 0.644}	
Ours	TSAD-C <sub>(1)</sub>	F1	0.709	0.623	0.540
		{Rec; APR}	{0.916; 0.772}	{0.800; 0.706}	{0.832; 0.649}
	TSAD-C <sub>(2)</sub>	F1	0.713*	0.661*	0.558
		{Rec; APR}	{0.894; 0.775}	{0.912; 0.738}	{0.936; 0.680}
TSAD-C <sub>(1,2)</sub>	F1	<b>0.747</b>	<b>0.680</b>	<b>0.572</b>	
	{Rec; APR}	{0.974; 0.789}	{0.943; 0.754}	{0.948; 0.700}	

Table 2: Comparison between existing methods and ours using F1, Rec and APR. The best and second-best F1 scores are denoted in bold and \*.

tential abnormal cases for further examination by medical experts to determine the appropriate course of action, while avoiding any missed abnormal cases as missing abnormal cases can have severe consequences, potentially leading to delayed treatment or opportunities for early intervention.

Moreover, while achieving high Rec, TSAD-C maintains reasonable APR and outperforms all unsupervised methods. Although supervised ones can achieve higher APR, they obtain much lower Rec. Supervised methods have access to more information, i.e. the labels of anomalies, in the training phase, yet TSAD-C outperforms them. Looking at the LSTM results in the Tables for the most challenging dataset, i.e., TUSZ, reveals that its F1 is equal to zero due to its poor performance in Rec. Note that  $\tau$  chosen in all methods is set to the one that provided the highest F1 on  $X_{\text{valid}}$ .

## Visualization of Normal Approximation

Figure 2 shows a visualization that compares the ground truth  $\mathbf{x}_{(i)}$ , decontaminated data  $\mathbf{x}_{(i)}^0$ , and reconstructed data  $\hat{\mathbf{x}}_{(i)}$  of a masked segment of normal and abnormal samples in DODH. The segment of the  $\mathbf{x}_{(i)}$  is masked to zeros, by applying BoM, before being processed by the Decontaminator. It is shown that  $\mathbf{x}_{(i)}^0$  and  $\hat{\mathbf{x}}_{(i)}$  fit  $\mathbf{x}_{(i)}$  very well in the normal case, leading to a lower  $s$ . Meanwhile, there are significant fluctuations of  $\mathbf{x}_{(i)}^0$  and  $\hat{\mathbf{x}}_{(i)}$  compared to  $\mathbf{x}_{(i)}$  in the abnormal case, resulting in a much higher  $s$ . This shows the effectiveness of TSAD-C in distinguishing anomalies from normal data.

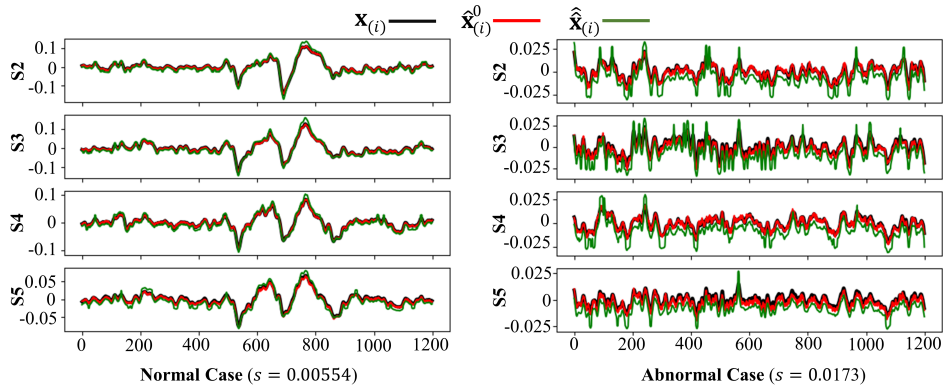


Figure 2: Comparison between normal and abnormal cases for the masked segment in DODH (S: Sensor). The masked strategy used is BoM. Each case includes  $\mathbf{x}_{(i)}$ ,  $\mathbf{x}_{(i)}^0$  and  $\hat{\mathbf{x}}_{(i)}$ .

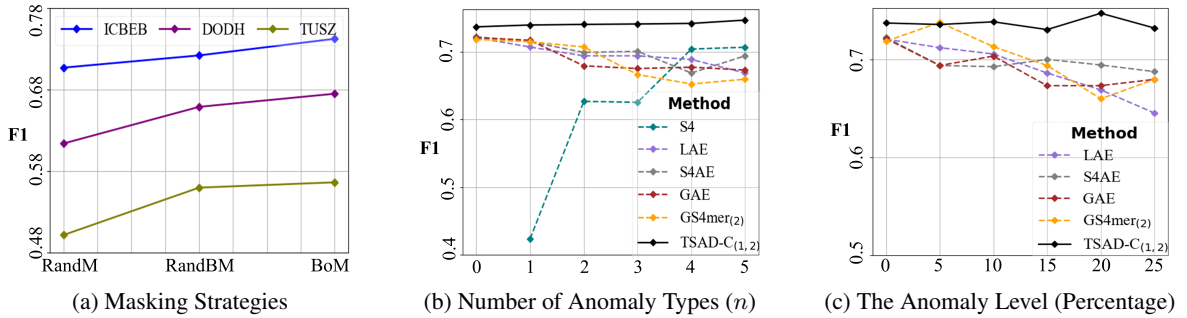


Figure 3: Hyper-parameter sensitivity analysis.

## Sensitivity Analysis

In this section, we investigate the effect of masking strategies on the performance of TSAD-C. Moreover, we conduct two additional settings of experiments for ICBEB: (1) changing the number of anomaly types in  $X_{\text{train}}$  and  $X_{\text{valid}}$ , and (2) changing the anomaly level in  $X_{\text{train}}$  and  $X_{\text{valid}}$ .

**Masking Strategies.** Figure 3a shows that BoM, which is a global masking where the same segment in  $\mathbf{x}_{(i)}$  is masked for all sensors, consistently achieves the higher F1 for all datasets compared to RandM and RandBM. This could be associated to the fact that masking the same segment across all sensors would be more suitable for implicitly learning of the shared patterns and relationships between sensors. Moreover, in our experiments, we observed that BoM results in a more stable and quicker convergence of the training phase.

**Effect of Variability on The Anomaly Types.** We assess the TSAD-C’s performance in detecting the five anomaly types available in  $X_{\text{test}}$  while not all anomaly types are present in  $X_{\text{train}}$  and  $X_{\text{valid}}$ . To this end, we introduce  $n$  as the number of anomaly types – e.g.,  $n = 2$  signifies two anomaly types present in  $X_{\text{train}}$  and  $X_{\text{valid}}$ . Note that the anomaly levels in  $X_{\text{train}}$  and  $X_{\text{valid}}$  remain constant. Figure 3b shows that the supervised methods (e.g., S4) can only achieve reliable results when all five anomaly types are present in  $X_{\text{train}}$  and  $X_{\text{valid}}$ . In contrast, the performance of unsupervised methods diminishes as  $n$  increases since they all assume the given input data as pure normal data,

hence are incapable of handling contaminated data. These methods face more difficulties when the input data impurity increases. Remarkably, TSAD-C consistently attains the highest F1, irrespective of changes in  $n$ . This underlines our method’s denoising prowess, as it remains effective regardless of the diversity in available anomaly types.

**Effect of Variability on The Anomaly Level.** We investigate the robustness of TSAD-C by varying the anomaly level. Note that all anomaly types are present within each subset of the dataset for this experiment. Figure 3c shows that TSAD-C exhibits consistent performance across different levels of anomalies, reinforcing the demonstration of the Decontaminator’s effectiveness in TSAD-C. Meanwhile, unlike TSAD-C, the performance of other unsupervised methods tends to decline as normal data impurity increases.

## Conclusion

This paper is the first attempt to provide a novel approach trained on contaminated data to detect anomalous observations in time-series data. The proposed method, called TSAD-C, consists of the Decontaminator, aiming to remove the potentially anomalous patterns in the training phase. Given decontaminated data, we propose the Variable Dependency Modeling to capture long-range intra- and inter-variable dependencies and provide an approximation of purified input data. An Anomaly Scoring module is achieved by integrating the capability of the two modules. We demon-

strate the outperformance of TSAD-C on three challenging MPS datasets compared to the existing methods.

## References

- Abubaker, M. B.; and Babayiğit, B. 2022. Detection of cardiovascular diseases in ECG images using machine learning and deep learning methods. *IEEE Transactions on Artificial Intelligence*, 4(2): 373–382.
- Alcaraz, J. M. L.; and Strodthoff, N. 2022. Diffusion-based time series imputation and forecasting with structured state space models. *arXiv preprint arXiv:2208.09399*.
- Berkaya, S. K.; Uysal, A. K.; Gunal, E. S.; Ergin, S.; Gunal, S.; and Gulmezoglu, M. B. 2018. A survey on ECG analysis. *Biomedical Signal Processing and Control*, 43: 216–235.
- Davis, J.; and Goadrich, M. 2006. The relationship between Precision-Recall and ROC curves. In *Proceedings of the 23rd international conference on Machine learning*, 233–240.
- Du, X.; Yu, J.; Chu, Z.; Jin, L.; and Chen, J. 2022. Graph autoencoder-based unsupervised outlier detection. *Information Sciences*, 608: 532–550.
- Ettahiri, H.; Ferrández Vicente, J. M.; and Fechtali, T. 2022. EEG brain signals to detect the sleep health of a driver: An automated framework system based on deep learning. *Frontiers in Human Neuroscience*, 16: 915276.
- Gao, J.; and Ribeiro, B. 2022. On the equivalence between temporal and static equivariant graph representations. In *International Conference on Machine Learning*, 7052–7076. PMLR.
- Gu, A.; Dao, T.; Ermon, S.; Rudra, A.; and Ré, C. 2020. Hippo: Recurrent memory with optimal polynomial projections. *Advances in neural information processing systems*, 33: 1474–1487.
- Gu, A.; Goel, K.; and Ré, C. 2022. Efficiently modeling long sequences with structured state spaces. In *International Conference on Learning Representations*.
- Guillot, A.; Sauvet, F.; During, E. H.; and Thorey, V. 2020. DREAM open datasets: Multi-scored sleep datasets to compare human and automated sleep staging. *IEEE transactions on neural systems and rehabilitation engineering*, 28(9): 1955–1965.
- Ho, T. K. K.; and Armanfard, N. 2023. Self-Supervised Learning for Anomalous Channel Detection in EEG Graphs: Application to Seizure Analysis. In *Proceedings of the AAAI Conference on Artificial Intelligence*, volume 37, 7866–7874.
- Ho, T. K. K.; Karami, A.; and Armanfard, N. 2023. Graph-based Time-Series Anomaly Detection: A Survey. *arXiv preprint arXiv:2302.00058*.
- Isin, A.; and Ozdalili, S. 2017. Cardiac arrhythmia detection using deep learning. *Procedia computer science*, 120: 268–275.
- James, C. J.; and Hesse, C. W. 2004. Independent component analysis for biomedical signals. *Physiological measurement*, 26(1): R15.
- Jia, Z.; Lin, Y.; Wang, J.; Zhou, R.; Ning, X.; He, Y.; and Zhao, Y. 2020. GraphSleepNet: Adaptive Spatial-Temporal Graph Convolutional Networks for Sleep Stage Classification. In *IJCAI*, volume 2021, 1324–1330.
- Jiang, X.; Liu, J.; Wang, J.; Nie, Q.; Wu, K.; Liu, Y.; Wang, C.; and Zheng, F. 2022. Softpatch: Unsupervised anomaly detection with noisy data. *Advances in Neural Information Processing Systems*, 35: 15433–15445.
- Katharopoulos, A.; Vyas, A.; Pappas, N.; and Fleuret, F. 2020. Transformers are rNNS: Fast autoregressive transformers with linear attention. In *International Conference on Machine Learning*, 5156–5165. PMLR.
- Khalkhali, V.; Shawki, N.; Shah, V.; Golmohammadi, M.; Obeid, I.; and Picone, J. 2021. Low Latency Real-Time Seizure Detection Using Transfer Deep Learning. In *2021 IEEE Signal Processing in Medicine and Biology Symposium (SPMB)*, 1–7. IEEE.
- Khayati, M.; Lerner, A.; Tymchenko, Z.; and Cudré-Mauroux, P. 2020. Mind the gap: an experimental evaluation of imputation of missing values techniques in time series. In *Proceedings of the VLDB Endowment*, volume 13, 768–782.
- Lim, S. H.; Erichson, N. B.; Hodgkinson, L.; and Mahoney, M. W. 2021. Noisy recurrent neural networks. *Advances in Neural Information Processing Systems*, 34: 5124–5137.
- Liu, F.; Liu, C.; Zhao, L.; Zhang, X.; Wu, X.; Xu, X.; Liu, Y.; Ma, C.; Wei, S.; He, Z.; et al. 2018. An open access database for evaluating the algorithms of electrocardiogram rhythm and morphology abnormality detection. *Journal of Medical Imaging and Health Informatics*, 8(7): 1368–1373.
- Loh, H. W.; Ooi, C. P.; Dhok, S. G.; Sharma, M.; Bhurane, A. A.; and Acharya, U. R. 2022. Automated detection of cyclic alternating pattern and classification of sleep stages using deep neural network. *Applied Intelligence*, 52(3): 2903–2917.
- Pradhan, A.; He, J.; and Jiang, N. 2022. Hand gesture recognition and biometric authentication using a multi-day dataset. In *Intelligent Robotics and Applications: 15th International Conference, ICIRA 2022, Harbin, China, August 1–3, 2022, Proceedings, Part IV*, 375–385. Springer.
- Rashed-Al-Mahfuz, M.; Moni, M. A.; Uddin, S.; Alyami, S. A.; Summers, M. A.; and Eapen, V. 2021. A deep convolutional neural network method to detect seizures and characteristic frequencies using epileptic electroencephalogram (EEG) data. *IEEE Journal of Translational Engineering in Health and Medicine*, 9: 1–12.
- Rath, A.; Mishra, D.; Panda, G.; and Satapathy, S. C. 2021. Heart disease detection using deep learning methods from imbalanced ECG samples. *Biomedical Signal Processing and Control*, 68: 102820.
- Shah, V.; Von Weltin, E.; Lopez, S.; McHugh, J. R.; Veloso, L.; Golmohammadi, M.; Obeid, I.; and Picone, J. 2018. The temple university hospital seizure detection corpus. *Frontiers in neuroinformatics*, 12: 83.
- Sohl-Dickstein, J.; Weiss, E.; Maheswaranathan, N.; and Ganguli, S. 2015. Deep unsupervised learning using nonequilibrium thermodynamics. In *International conference on machine learning*, 2256–2265. PMLR.

Strodthoff, N.; Wagner, P.; Schaeffter, T.; and Samek, W. 2020. Deep learning for ECG analysis: Benchmarks and insights from PTB-XL. *IEEE Journal of Biomedical and Health Informatics*, 25(5): 1519–1528.

Tang, S.; Dunnmon, J.; Saab, K. K.; Zhang, X.; Huang, Q.; Dubost, F.; Rubin, D.; and Lee-Messer, C. 2021. Self-Supervised Graph Neural Networks for Improved Electroencephalographic Seizure Analysis. In *International Conference on Learning Representations*.

Tang, S.; Dunnmon, J. A.; Liangqiong, Q.; Saab, K. K.; Baykaner, T.; Lee-Messer, C.; and Rubin, D. L. 2023. Modeling Multivariate Biosignals With Graph Neural Networks and Structured State Space Models. In *Conference on Health, Inference, and Learning*, 50–71. PMLR.

Tao, J. X.; Ray, A.; Hawes-Ebersole, S.; and Ebersole, J. S. 2005. Intracranial EEG substrates of scalp EEG interictal spikes. *Epilepsia*, 46(5): 669–676.

Thodoroff, P.; Pineau, J.; and Lim, A. 2016. Learning robust features using deep learning for automatic seizure detection. In *Machine learning for healthcare conference*, 178–190. PMLR.

Thuwajit, P.; Rangpong, P.; Sawangjai, P.; Autthasan, P.; Chaisaen, R.; Banluesombatkul, N.; Boonchit, P.; Tatsaringkansakul, N.; Sudhawiyangkul, T.; and Wilaiprasitporn, T. 2021. EEGWaveNet: Multiscale CNN-Based Spatiotemporal Feature Extraction for EEG Seizure Detection. *IEEE Transactions on Industrial Informatics*, 18(8): 5547–5557.

Vaswani, A.; Shazeer, N.; Parmar, N.; Uszkoreit, J.; Jones, L.; Gomez, A. N.; Kaiser, Ł.; and Polosukhin, I. 2017. Attention is all you need. *Advances in neural information processing systems*, 30.

Wang, P.; Jiang, A.; Liu, X.; Shang, J.; and Zhang, L. 2018. LSTM-based EEG classification in motor imagery tasks. *IEEE transactions on neural systems and rehabilitation engineering*, 26(11): 2086–2095.

Wei, Y.; Jang-Jaccard, J.; Xu, W.; Sabrina, F.; Camtepe, S.; and Boulic, M. 2023. LSTM-autoencoder-based anomaly detection for indoor air quality time-series data. *IEEE Sensors Journal*, 23(4): 3787–3800.

Xu, K.; Hu, W.; Leskovec, J.; and Jegelka, S. 2019. How powerful are graph neural networks? In *International Conference on Learning Representations*.

Xu, S.; Faust, O.; Silvia, S.; Chakraborty, S.; Barua, P. D.; Loh, H. W.; Elphick, H.; Molinari, F.; and Acharya, U. R. 2022. A review of automated sleep disorder detection. *Computers in Biology and Medicine*, 106100.

Zhang, H.; Wang, Z.; Wu, Z.; and Jiang, Y.-G. 2023. DiffusionAD: Denoising Diffusion for Anomaly Detection. *arXiv preprint arXiv:2303.08730*.

Zhu, Y.; Xu, W.; Zhang, J.; Du, Y.; Zhang, J.; Liu, Q.; Yang, C.; and Wu, S. 2021. A survey on graph structure learning: Progress and opportunities. *arXiv preprint arXiv:2103.03036*.